Tunable Gamma-Rays in a Thermal Fission Environment for Microelectronics Testing

M. Niichel & S. Chatzidakis

***Abstract*—This work develops a method to tailor the radiation environment of a low-power thermal research reactor to enable earlier, lower-cost screening during microelectronic design. Test casings of pure copper, indium, and cadmium, and of the same metals suspended in paraffin, were selected using a first-principles figure of merit that weights prompt (n,γ) emission by the mass energy-absorption coefficient of silicon, then modeled in MCNP6.3 and irradiated in the Purdue University Reactor Number One (PUR-1). Photon dose in silicon, derived from TLD-600/700 pairs via Burlin cavity theory, and 1-MeV equivalent fluence, obtained from foil activation and SAND-II unfolding, show that the casings tune the gamma-to-neutron balance across a factor of seven, from 39× to 278× the ratio permitted by MIL-STD-883, with the best configuration delivering 32 rad(Si)/s at full reactor power. Because the drop tube at its present location is already gamma-dominated by a factor of 46 without any casing, this position can serve only as a total ionizing dose source and cannot supply a compliant displacement damage environment. Threshold voltage shifts measured in BSS119N MOSFETs irradiated using each test casing correlate more strongly with thermal neutron fluence ($R^2 = 0.94$) than with the measured photon dose ($R^2 = 0.46$), and cadmium shielding that removes 97% of the thermal fluence also removes 42% of the threshold shift. These results indicate that thermal neutrons contribute ionizing dose local to the device that externally placed dosimetry does not register, and that spectrum-hardening practices intended to approximate a 1-MeV equivalent environment may discard a substantial portion of the dose a device actually receives.**

***Index Terms*—Radiation testing, Total ionizing dose, Neutron spectrum tailoring, Gamma production, MCNP6.3, PUR-1 reactor, Radiation-hardened electronics, Gamma dose enhancement**

I. Introduction

Radiation testing of microelectronics is essential for systems operating in space or nuclear reactor facilities, but it is both time-intensive and costly. Qualification as a radiation-hardened system under MIL-STD-883 requires exposure to 50–2000 rad(Si)/s total dose rate of Co-60 and 1 MeV-equivalent neutron fluence. The version approved in 2013, specifies that a neutron source should not exceed 500 rad(Si) per 1×10^{12} n/cm^2 fluence. Domestic testing capacity adhering to these requirements struggles to meet current demand for mid- to low-budget projects, with some facilities booked up to two years in advance. The chief concern for small microelectronic projects is spending the time and money on the design all to have them fail initial testing to meet the MIL-STD. Failure often comes down to a component that requires redesigns, further extending development timelines.

After the divestment of radiation testing facilities following the 1990s, demand remained low for commercial hardness assurance testing until the mid-2010s when both nuclear power and space-based assets started becoming mainstream once more [1]. A joint-agency commissioned report determined that the 2030 domestic demand for radiation assurance testing will far exceed projected capacity [1]. As a result, alternative test methods are needed to relieve pressure on the existing infrastructure.

During preparation for radiation testing of an STM32-based system in accordance with the MIL-STD-883 neutron and total ionizing dose (TID) standards, we found that scheduling a facility that met the timeline or could accommodate the experimental setup was difficult [2]. As an example, a Co-60 irradiator located in the vicinity of Purdue University was approaching an age where the activity could not meet the 50-2000 rad(Si)/s for TID. Similarly, several other facilities relatively near the university did not have an irradiator that could accommodate measurement cables for the experimental setup despite meeting the dose rate. Also related, the White Sands Missile Range Fast Burst Reactor (FBR) was available, but only as an in-kind rider on a higher-priority test campaign. Unfortunately, the reactor power requirements for the supporting experiment did not produce a neutron flux large enough to induce failures in the lower priority experiment over the 1-hour exposure time permitted by the FBR's staff. Despite receiving time in a facility that could meet the MIL-STD testing, experimental constraints prevented the collection of useful data. This experience is not atypical for experimenters desiring radiation testing for their systems.

While, the Purdue subcritical pile and 10-kW research reactor (PUR-1) are not a TRIGA or FBR as outlined by the MIL-STD, their availability and ability to collapse *via* damage function folding to 1-MeV equivalent neutron fluence (Si) provided the opportunity to assess if the device under test (DUT) had any resilience against neutrons [3]. In an effort to tailor the highly thermalized PUR-1 neutron spectrum closer to that of a standard 1-MeV equivalent source, a 1-mm thick 3N (99.9% purity) cadmium shield was placed around the DUT. The results were compared to a similar DUT placed in the bare PUR-1 environment (control) and a MIL-STD compliant Co-60 environment hosted by Naval Surface Warfare Command Crane Division [4]. It was observed that the response of the DUT surrounded with cadmium exhibited electronic behavior more in line with the Co-60 DUT than the bare PUR-1 device. The observation is indicative of a strong dependence on TID and suggests that the capture gammas from the Cd-113(n,γ)Cd-114 reaction increased the gamma dose rate relative to the bare environment. This was further supported by TLD

measurements [4, 5].

Radiation testing in PUR-1 suggests that it may be possible to use a shield composed of materials with a high affinity for neutrons to tune the energy of effluent gammas such that their interaction with silicon-based microelectronics is optimal for any given neutron spectrum. While this type of testing is not intended to replace the current hardness assurance requirement for a TRIGA or FBR, it may be useful as an accessible and cost-effective supplement for low-level testing earlier in the microelectronic design process. In this work, we propose a method for selecting the neutron-absorbing material to optimize gamma production, in order to tune the thermal fission environment closer to that of a device's intended operational conditions. We compare the first-principles-derived algorithm to MCNP6.3 and experimental results derived through metal foil activation in line with ASTM E720-23 and lithium-fluoride (LiF) TLD 600/700 measurements in line with ASTM E668-20 [6, 7].

II. Background

The National Ignition Facility coequally known as NIF, is one of many domestic efforts for developing the viable use of fusion technology. Their facility hosts numerous sub-facilities that conduct nuclear experiments. One such experiment is the ATHENA energy tuning assembly. A chamber with specifically designed material composition for down scattering fusion neutrons into a thermonuclear plus prompt fission neutron spectrum [8]. This particular radiation environment is the basis of the Co-60 and 1-MeV equivalent fluence requirement of the military standard for testing microelectronics [9, 10].

A related PhD dissertation published in 2017 out of UC Berkeley discusses the development of the ATHENA facility. Bevins describes the use of MCNP to narrow down the material selection of the tuning assembly. Then presents foil activation kits containing various metals and the subsequent use of the Pacific Northwest National Laboratory's STAYSL code for neutron spectrum unfolding. The result of the dissertation provides a recommendation for material composition for the ATHENA at the NIF [11].

The Air Force Institute of Technology has made use of ATHENA as recently as 2022 for conducting microelectronic survivability tests on transistor technologies. In Kloppenburg's report, he compares the damage of the 2N2222 bipolar transistor (BJT) between the Ohio State research reactor and the ATHENA facility at NIF. The hypothesis states that the post-irradiation measurements of the BJT will be the same regardless of neutron energy, but the dynamic measurements during irradiation will vary due to different damage mechanisms. Evidence in support of the hypothesis is presented in the thesis, showing that post-irradiation effects are independent of neutron energy; however, dynamic measurements are not [12]. It is mentioned that gamma rays were not considered in this work, for either the reactor or ATHENA.

A complementary finding from Kloppenburg was noted by work conducted by Niichel *et al.* when testing the BSS119N MOSFET in PUR-1. Niichel's work attempts to classify the effects of gamma rays and neutrons separately [4]. Evidence suggests that the energy of the neutrons does affect the post-irradiation effects by shifting the threshold voltages of the MOSFET. It should be noted that BJTs and MOSFETs diverge in the primary damage mechanism, where MOSFETs tend to be more sensitive to TID than their BJT counterpart [13]. Regardless, it was proposed that thermal neutrons induce activations internal to the device, ultimately delivering additional TID that goes unaccounted for when dosimetry is not placed with the DUT. This report aims to further investigate the effects of thermal neutron-induced gammas on a DUT and maximize the effect for radiation testing.

III. Material Selection

The selection of the material followed four categories in order of precedence. First, the material must have a relatively large microscopic cross-section for the (n, γ) reaction. Second, if the material did not provide a prompt gamma, the half-life of the isotope must be small compared to the irradiation time to allow for build-up to occur. Third, the material should provide a high-energy gamma, such that attenuation in most materials is unlikely. Finally, the material needs to be accessible. Meaning cost and shipping times are subjectively reasonable for the project's budget.

The physical dimensions of the converter must optimize three material properties to achieve maximum photon yield at the test location. The first is a large cross-section for absorption, though this was already accounted for in the material selection. The second is neutron scattering, specifically the average logarithmic energy decrement per collision (ξ). It is of interest to thermalize neutrons, but not to prematurely absorb low-energy neutrons at a thickness where subsequent photons will be attenuated. Finally, the linear mass attenuation of the conversion material must be such that it transmits photons of energies produced from the capture reactions. For the proposed model, the full span of the differential neutron energy spectrum need not be defined; the relative ratio of fast to thermal flux should be estimated. However, the testing location's volumetric capacity should be known, as this is a material optimization input parameter. In the case of PUR-1, the 7.6 cm drop tube constrains the thickness of any shielding layer placed between the tube wall and the DUT [14].

To address the material optimization for the PUR-1 test tube, five designs are considered: an unconstrained layered design using wax followed by a metal sheet, an unconstrained mixture of wax and powdered metal at 20% by weight, a space-limited layered design, a space-limited powdered metal and wax, and a pure metal sheet. If any optimal thickness exceeds the capacity of the drop tube, including DUT volume, that design is excluded.

A. Layered Wax and Metal Sheet Test Casing Design

Considering the first design, a layer of wax (converter A) will be used to thermalize epithermal neutrons and above. The optimal length balances thermal neutron production with thermal neutron absorption. Then the metal layer (converter B) will be placed for the conversion of neutrons to gammas, balancing gamma production and attenuation.

The following equation describes the fast neutron flux loss following an exponential attenuation due to scattering and removal from the fast group, so that the flux obeys

$$\frac{d\phi_f(x)}{dx} = -k_A\phi_f(x) \Longrightarrow \phi_f(x) = \phi_{f,0}\, e^{-k_A x} \quad (1)$$

where $\phi_{f,0}$ is the initial incident fast neutron flux and k_A is an effective fast-to-thermal conversion coefficient. The conversion coefficient is defined as

$$k_A = \frac{\xi\Sigma_s}{\ln\left(\frac{E_0}{E_{th}}\right)} \quad (2)$$

where ξ is the average logarithmic energy decrement per collision, Σ_s is the macroscopic scattering cross section of converter A, E_0 is the average incident fast neutron energy, and E_{th} is the thermal neutron energy.

Thermal neutrons are produced via down-scattering of fast neutrons and are lost through absorption and leakage. The thermal neutron flux $\phi_{th}(x)$ satisfies the balance equation

$$\frac{d\phi_{th}(x)}{dx} = k_A\phi_f(x) - a_A\phi_{th}(x) \quad (3)$$

in which the effective thermal loss coefficient is defined as

$$a_A = \Sigma_{a,th} + \alpha_{\text{leak}} \quad (4)$$

where $\Sigma_{a,th}$ is the macroscopic thermal absorption cross section, and the leakage term is modeled using the transport-diffusion approximation [15]. This approximation is given by

$$\alpha_{\text{leak}} = DB^2, \qquad D = \frac{1}{3\Sigma_{tr}} \quad (5)$$

with D acting as the diffusion coefficient, $\Sigma_{tr}$the macroscopic transport cross section, and B^2 the geometric buckling. Solving the coupled fast–thermal system yields the thermal neutron flux exiting converter A. The thermal flux acting as the incident thermal flux into converter B is estimated by

$$\phi_{th}^{B,in}(L_A) = \phi_{th,0}\, e^{-a_A L_A} + \phi_{f,0}\frac{k_A}{a_A - k_A}(e^{-k_A L_A} - e^{-a_A L_A}) \quad (6)$$

It is often convenient to define the fast-to-thermal flux ratio as

$$r = \frac{\phi_{f,0}}{\phi_{th,0}} \quad (7)$$

so that the converter thickness that maximizes the thermal neutron flux at the exit of converter A follows from setting the derivative of Equation (6) to zero, which gives

$$\frac{d\phi_{th}^{B,in}(L_A)}{dL_A} = 0 \Longrightarrow L_{A,opt} = \frac{1}{a_A - k_A}\ln\left(\frac{a_A(k_A(r+1) - a_A)}{r\,k_A^2}\right) \quad (8)$$

which is subject to the constraint that

$$k_A(r+1) - a_A > 0 \quad (9)$$

The performance of converter A is quantified using a normalized figure of merit

$$FOM_A = \frac{\phi_{th}^{B,in}(L_A)}{\phi_{th,0}} \quad (10)$$

which is maximized at $L_{A,\,opt}$. This term captures the efficiency of converting incident fast and thermal neutrons into useful thermal neutrons delivered to converter B. Converter B is designed to capture thermal neutrons and emit prompt gamma rays that escape toward the silicon target.

The thermal neutron flux in converter B decays exponentially due to neutron capture by way of

$$\phi_{th}^{B}(x) = \phi_{th}^{B,in}\, e^{-\Sigma_{a,B}x} \quad (11)$$

where $\Sigma_{a,B}$ is the macroscopic thermal neutron absorption cross section of converter B.

A prompt gamma ray of energy E_i that is produced at depth x must traverse a distance $L_B - x$ to escape the converter. Where i indexes the prompt gamma lines of the capture cascade in converter B and is carried over into the escape probability

$$P_{esc,i}(x) = e^{-\mu_B(E_i)(L_B - x)} \quad (12)$$

where μ_B is the linear gamma attenuation coefficient of converter B evaluated at the prompt gamma energy (E_i). The gamma current exiting converter B is obtained by integrating the local capture rate weighted by the escape probability

$$J_\gamma(L_B) = \sum_i \Sigma_{\gamma,i}\int_0^{L_B}\phi_{th}^{B}(x)\, P_{esc,i}(x)\, dx \quad (13)$$

Substituting equations (11) and (12) gives

$$J_\gamma(L_B) = \phi_{th}^{B,in}\sum_i \Sigma_{\gamma,i}\int_0^{L_B} e^{-\Sigma_{a,B}x}\, e^{-\mu_B(E_i)(L_B - x)}\, dx \quad (14)$$

where the figure of merit for converter B is

$$\text{FOM}_B = \sum_i \Sigma_{\gamma,i}\, E_i\left(\frac{\mu_{en}(E_i)}{\rho}\right)_{\text{Si}}\int_0^{L_B} e^{-\Sigma_{a,B}x}\, e^{-\mu_B(E_i)(L_B - x)}\, dx \quad (15)$$

Where $(\mu_{en}/\rho)_{\text{Si}}$ is the mass energy-absorption coefficient of silicon indexed for energy. The optimized length solved numerically ($L_{B,\,opt}$) follows

$$\frac{dFOM_B}{dL_B} = 0 \Longrightarrow L_{B,\ opt} \quad (16)$$

The total performance of the layered converter is provided by

$$FOM_{total} = FOM_A \cdot FOM_B \quad (17)$$

This expression is proportional to the gamma-induced dose rate in silicon per unit incident thermal neutron flux. The optimal total thickness of the layered design is therefore simply the sum of the two optimized layer thicknesses,

$$L_{total,opt} = L_{A,opt} + L_{B,opt} \quad (18)$$

B. Wax and Metal Powder Mixture Test Casing Design

A similar analysis can be performed for the wax and metal powder type design. For the fast neutron flux $\phi_f(x)$ in the mixture is modeled as exponential attenuation in

$$\phi_f(x) = \phi_{f,0}e^{-k_m x} \quad (19)$$

where $\phi_{f,0}$is the incident fast neutron flux at $x = 0$, and $k_m = (1-f)k_A$ is an effective fast-to-thermal conversion/removal coefficient of the mixture [cm^{-1}] (analogous to $k_A$in the layered case) with *f* the volume fraction of component B. The thermal neutrons are produced by down-scattering of the fast flux and are lost through thermal absorption and leakage. The resulting thermal flux at the thickness *L* is shown in

$$\phi_{th}(x) = \phi_{th,0}\, e^{-a_m x} + \phi_{f,0}\frac{k_m}{a_m - k_m}(e^{-k_m x} - e^{-a_m x}) \quad (20)$$

where $\phi_{th,0}$is the incident thermal neutron flux at $x = 0$, and $a_m$is the effective thermal loss coefficient of the mixture provided by

$$a_m = \Sigma_{a,th,\text{mix}} + \alpha_{\text{leak,mix}},\ \alpha_{\text{leak,mix}} = D_{\text{mix}}B^2, D_{\text{mix}} = \frac{1}{3\Sigma_{tr,\text{mix}}} \quad (21)$$

with $\Sigma_{a,th,\text{mix}} = (1-f)\Sigma_{a,A} + f\Sigma_{a,B}$ [1]. The entrance fast-to-thermal ratio *r* is defined similarly to the layered converter case. Thermal neutron capture in the mixture produces prompt gammas. The inclusion of the wax introduces a non-negligible amount of hydrogen that produces a capture gamma ray of 2.2 MeV; this is accounted for in each metal selection through

$$\Sigma_{\gamma,\text{mix},i} = \begin{cases} f\,\Sigma_{\gamma,B,i}, & i \in \text{metal cascade} \\ (1-f)\,N_H\sigma_{\gamma,H}, & i = \text{H},\ E_i = 2.22\ \text{MeV} \end{cases} \quad (22)$$

where N_H is the atomic density and $\sigma_{\gamma,H}$ is the neutron capture cross-section (0.33 b) of hydrogen. If the macroscopic partial gamma-ray production cross section for cascade line i is $\Sigma_{\gamma,\mathrm{mix},i} = f\,\Sigma_{\gamma,B,i}\Sigma_{\gamma,\ \mathrm{mix,i}} = f\ \Sigma_{\gamma,\mathrm{B,i},}$ then the escaping gamma current from the exit face at $x = L$ adheres to the following

$$J_\gamma(L) = \sum_i \Sigma_{\gamma,\mathrm{mix},i} \int_0^L \phi_{th}\,(x)\, e^{-\mu_m(E_i)(L-x)}\, dx \qquad (23)$$

where $e^{-\mu_m(L-x)}$ is the escape probability for a gamma produced at depth x, and $\mu_m = (1-f)\mu_A + f\mu_B$, is the linear gamma attenuation coefficient of the mixture evaluated at the prompt gamma energy. Carrying out the integral produces

$$J_\gamma(L) = \sum_i \Sigma_{\gamma,\mathrm{mix},i} \int_0^L [\,\phi_{th,0}\, e^{-a_m x} + \phi_{f,0} \frac{k_m}{a_m - k_m} \times (e^{-k_m x} - e^{-a_m x}) \times e^{-\mu_m(E_i)(L-x)}\, dx \qquad (24)$$

This expression captures the competing effects of (i) increased thermal production and capture volume with increasing L and (ii) self-attenuation of prompt gammas as L increases. The mixture converter figure of merit is defined to be proportional to silicon dose rate via the emitted gamma energy and silicon energy absorption from

$$\mathrm{FOM_{mix}} = \sum_i \Sigma_{\gamma,\mathrm{mix},i}\ E_i \left(\frac{\mu_{en}(E_i)}{\rho}\right)_{\mathrm{Si}} \int_0^L \phi_{th}\,(x)\, e^{-\mu_m(E_i)(L-x)}\, dx \qquad (25)$$

where E_i is the prompt gamma energy and $(\mu_{en}/\rho)_{\mathrm{Si}}$ is the mass energy-absorption coefficient of silicon at E_γ. The optimal mixture thickness $L_{\mathrm{mix,opt}}$ is obtained by

$$\frac{d\ \mathrm{FOM_{mix}}}{dL} = 0 \Longrightarrow L_{\mathrm{mix,opt}} \qquad (26)$$

which can be solved numerically since $J_\gamma(L)$ contains multiple exponential terms with different attenuation constants (k_m, a_m, μ_m).

The ENDF/B-VIII.0 cross-section library is used to provide the input parameters for the above-described algorithm for selected materials at 0.025 eV. However, for metals like copper, where there are two isotopes that have a high affinity for neutrons, a combined data set can be generated by summing the isotope indices together as a function of incident neutron energy. While cadmium has several stable isotopes, the cross-section for Cd-113 is four orders of magnitude larger than the other isotopes, and is therefore the dominating effect. Indium also has two stable isotopes, with a similar cross-section; however, In-113 has an abundance of less than 5%. Therefore, the effect is strongly correlated with In-115. Finally, copper has two isotopes with similar cross-sections, but the Cu-63 and Cu-65 abundances are 69.2% and 30.9%, respectively. Therefore, both must be considered. The cross-section data for Cd-113, In-115, and Cu-63/65 are plotted in Fig. 1. Although all of these isotopes subsequently decay into other materials, the timeline of the test is small compared to the buildup of other isotopes; thus, they can be neglected. The prompt gamma production from the (n,γ) reactions for Cu, In, and Cd is overlaid on the mass-energy absorption as a function of photon energy in silicon in Fig. 2, Fig. 3, and Fig. 4, respectively.

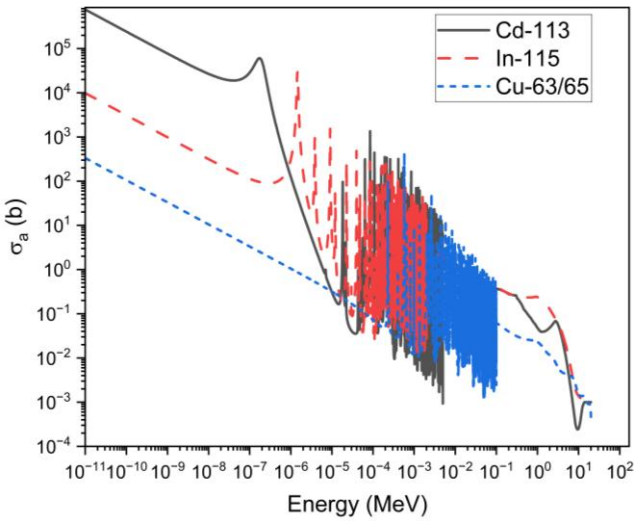

Fig. 1. ENDF/VIII.0 microscopic cross-section for absorption and production of gamma energy of selected metals as a function of energy [16 - 19].

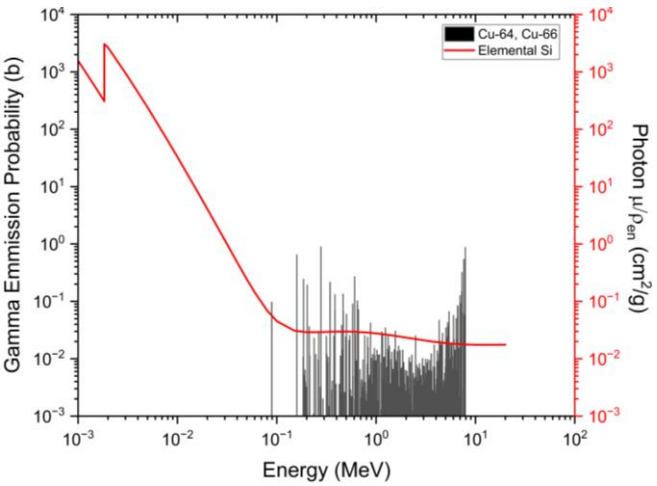

Fig. 2. Mass-energy absorption coefficients in elemental silicon for the prompt gammas produced from the neutron capture in copper [20, 21].

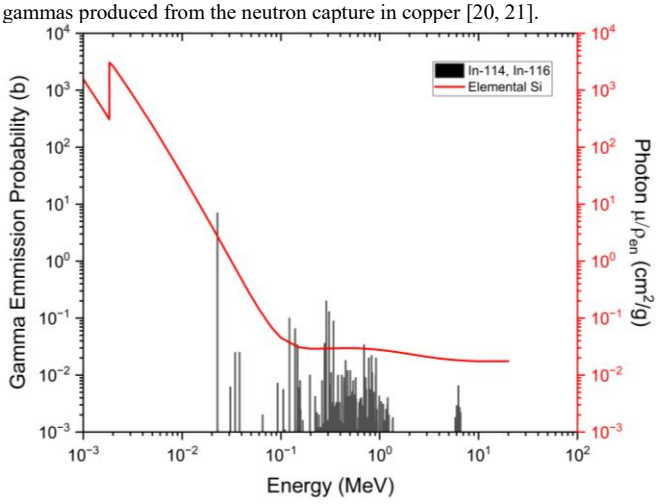

Fig. 3. Mass-energy absorption coefficients in elemental silicon for the prompt gammas produced from the neutron capture in indium [20, 21].

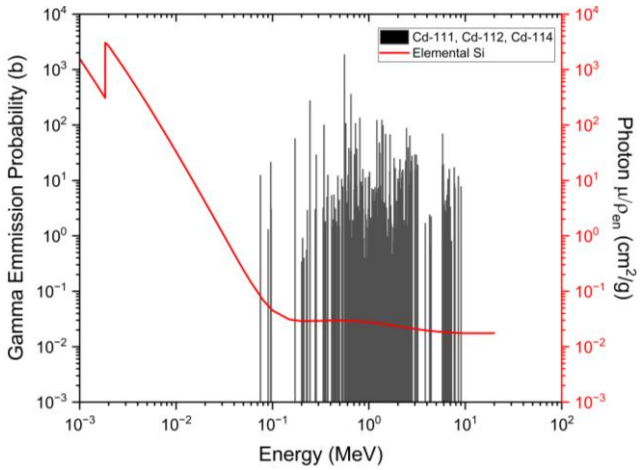

Fig. 4. Mass-energy absorption coefficients in elemental silicon for the prompt gammas produced from the neutron capture in cadmium [20, 21].

Before any neutron spectrum measurement was taken of PUR-1, a fast-to-thermal ratio was estimated at 0.02 for input into the algorithm. This value was based on the location of the drop tube from the core face (30.00 cm) and a pair of gold foils consisting of one bare foil and one cadmium-covered foil. Additionally, 0.6 cm was reserved for the conversion materials to allow for a DUT. One key detail that should be noted is that the wax mixture models consider the gamma contribution from hydrogen absorption of thermal neutrons, which produces a 2.2 MeV photon, but the layered design does not include this gamma energy. A non-negligible contribution to the dose comes from hydrogen capture. In the wax mixtures, the majority of the material's macroscopic cross-section is dominated by the wax. The inclusion of a metal sheet in the layered design shifts the dominance of the macroscopic cross-section to the metal. Regardless, due to the selected thermal field in PUR-1, the space-constrained layered designs are optimal with no wax and are effectively a pure metal sheet. Thus, the hydrogen dose contribution is irrelevant for modeling PUR-1. For the given input parameters, the two designs being compared were the space-constrained wax mixtures at 20% metal doping and the optimized space-constrained layered design. The comparison of the FOM_{total} for each material is shown in Fig.5.

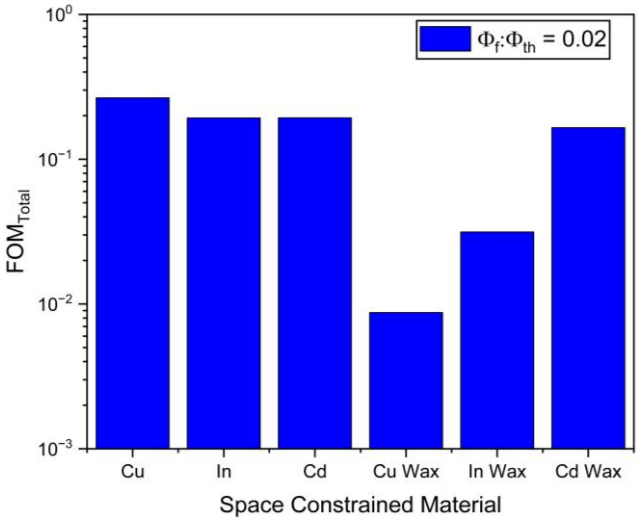

Fig. 5. Comparison of the total figure of merit for the space-constrained layered and mixture designs in a highly thermalized neutron spectrum. Note that, for the given input parameters, the layered design minimized layer A (wax) to zero, effectively establishing a pure metal sheet at 0.6 cm thickness.

The results of the above algorithm suggest that for the conditions in PUR-1, the best-performing material is the copper sheet, followed by indium and cadmium sheets. Whereas the wax mixture models follow the order of increasing thermal neutron cross-section. What is not included in any of the designs is the contribution from delayed gamma rays. Where indium and copper are speculated to be major sources of delayed gamma ray production due to their relatively short half-lives. Indium in particular has a half-life of approximately 52 minutes, and it is reasonable to assume that saturation activity could be achieved during a standard irradiation test. The approximately 12-hour half-life for copper-64 is less likely to achieve saturation, but remains a significant contribution to dose.

IV. MCNP Simulation

The Purdue reactor is a 10 kW pool-type core loaded with HALEU fuel [22]. The work conducted by Miller *et al.* and Townsend provides in detail the dimensional characteristics for the reactor and auxiliary equipment [14, 22]. It is with this information that the geometry of the drop tube can be modeled in MCNP6.3 for comparison with the algorithm derived from first principles.

Ultimately, the region of interest in the geometry exists within the drop tube centerline with the core. As a result, the core can be treated as a homogeneous rectangular parallelepiped of aluminum, and the fission environment can be established with an MCNP SDEF card for irradiation. The particle energy and probabilities for U-235 fission can be found in a Lawrence-Livermore report from 2010 [23]. While the specific fuel composition of PUR-1 is not pure U-235, it is assumed that the energy spectrum for neutrons and gammas remains unaffected. The normalized neutron lethargy (ranging from 5.50×10^{-10} – 1.85×10^{1} MeV) at the core center and the drop tube are displayed in Fig. 6, and the normalized photon distribution for the same is displayed in Fig. 7. Normalizing these values allows for a comparison of the spectrum hardness between the two locations.

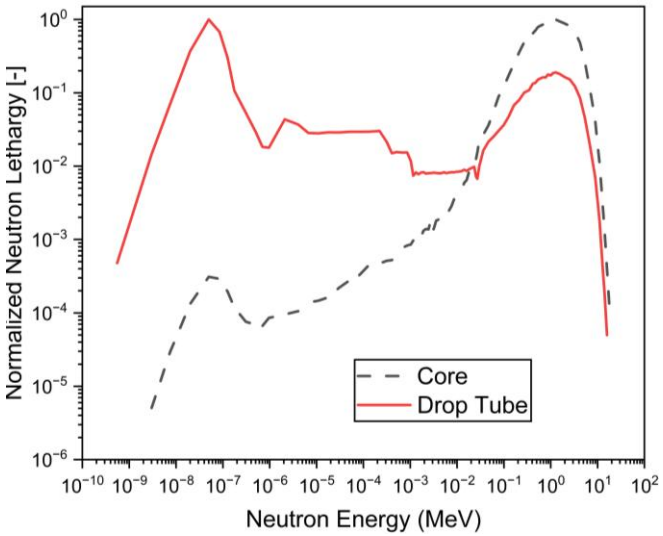

Fig. 6. Comparison of neutron energy spectra at the core boundary and in the center of the drop tube within PUR-1. Normalized to 1 to compare the hardness of each spectrum.

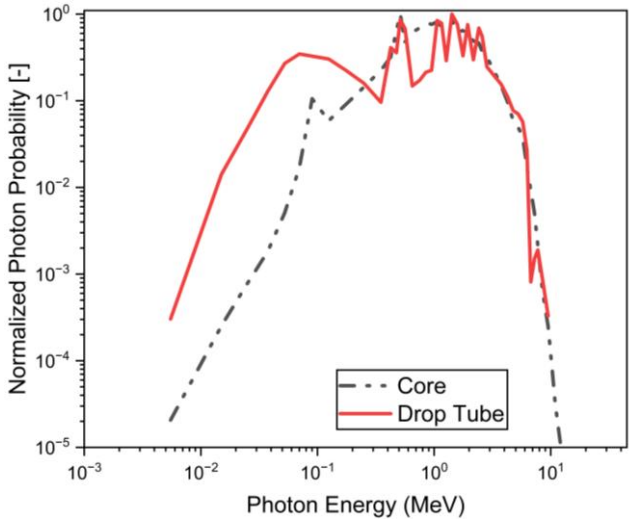

Fig. 7. Comparison of photon energy spectra at the core boundary and in the center of the drop tube within PUR-1. Normalized to 1 to compare the hardness of each spectrum.

The test casings are modeled inside a polylactic acid 3D-printed capsule with a wall thickness of 1.27 cm. Outside of MCNP, the capsule serves as a vessel to contain activated materials and to ensure that parts to be irradiated are easily placed/removed from the drop tube during experiments. One current challenge is that 3D printing filament uses pigments that are not tightly regulated. The chemical composition of pigment ranges between 1-3% wt., and can have metal compounds ranging from iron to uranium [24]. It is assumed that no pigment is added. An experimental setup should be consistently maintained among various filament colors for the drop tube capsules. This will help prevent unsuspecting material activation, but future work may be warranted on the filament itself [25].

Each of the test casings was modeled as a 0.6-cm thick sheet on the interior of the capsule, and F4 tallies were used for tracking neutrons and photons at the center of the testing location. The DUT simulated in MCNP was a cylindrical slug of elemental silicon with a 1.93 cm radius to represent a general microelectronic system. F4 and F6 tallies were placed in this cell and are the tallies of interest to observe the shift from replacing the various test casing materials. One note related to the wax design is that MCNP did not have a material data card to handle the thermal scattering [S(α, β)] of paraffin wax. As a result, the S(α, β) card for high-density polyethylene was used. This material treatment choice underestimates the S(α, β) in wax by up to 20% for energies below 0.5 eV [26]. Light water and the HDPE drop tubes were assigned to the correct thermal scattering library.

The MCNP-generated gamma and neutron spectra for the pure metal models are compared to the control (bare reactor) in Fig. 8 and Fig. 9, respectively. While the same is plotted in Fig. 10 and Fig. 11 for the wax models. Separating the two designs allows for visual clarity. The particle history was set to 5.0×10^{8} source particles, producing a tally uncertainty of 7.0×10^{-3} for the F4, and 1.0×10^{-4} for the F6 tallies. While the plotted spectra do have error bars, they are indistinguishable from the lines. The random number generator was set to the 4th generation, with a seed value of 2147483647 and a stride value of 11973779.

Considering the F4 results, the pure metals have a larger photon deviation from the bare drop tube environment compared to the wax composites. This is also true for the neutron shift. The addition of wax at 80% by weight means that it dominates the nuclear reactions. It should be noted that the ratio of metal powder to wax was selected rather arbitrarily, but foreknowledge of doping plastics with denser materials has proved challenging to achieve a homogeneous end product. Thus, the 20% loading was selected to make manufacturing feasible. Nonetheless, the F4 tallies give the appearance that this loading fraction is not sufficient to modify the neutron or photon spectrum nearly as much as the pure metals. As a result, the F6 tallies placed in the silicon slug provide a more complete picture of the energy deposited for each environment. The F6 tallies are proportional to KERMA and, under the charged particle equilibrium assumption, dose. The F6 tallies generated through MCNP are plotted in Fig. 12, and the relative change from the bare PUR-1 for neutrons and photons is in Table I.

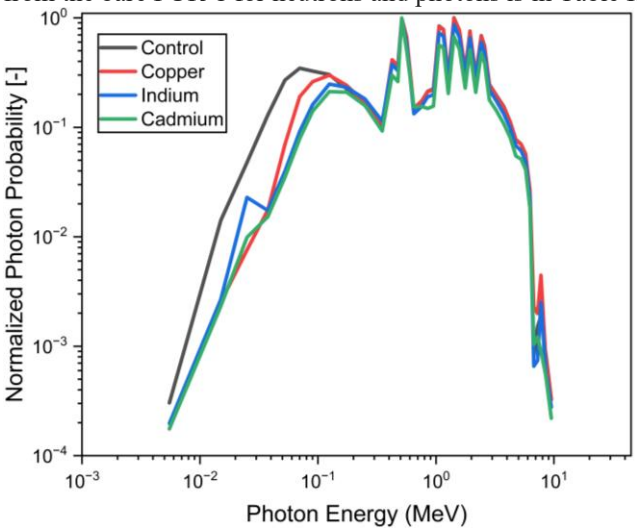

Fig. 8. Comparison of MCNP photon spectra in the drop tube location for the selected metals. Normalized to 1 to compare the hardness of each spectrum.

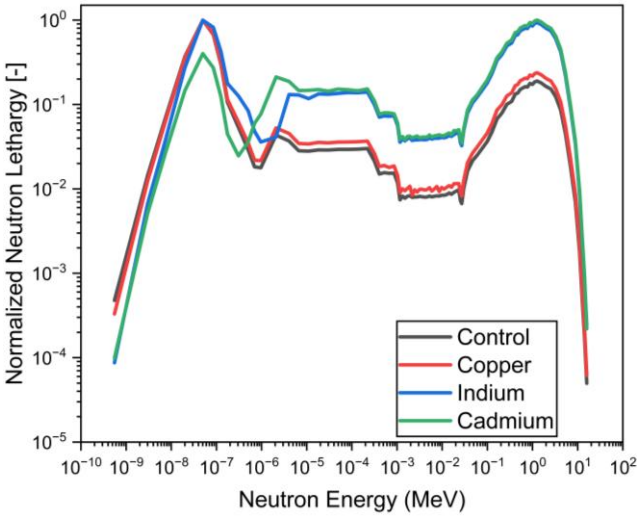

Fig. 9. Comparison of MCNP-generated neutron spectra in the drop tube location for the selected metals. Normalized to 1 to compare the hardness of each spectrum.

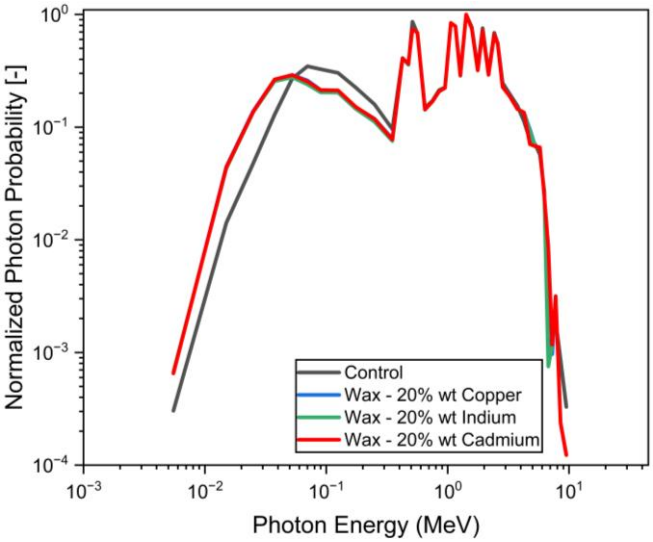

Fig. 10. Comparison of MCNP-generated photon spectra in the drop tube location for 20% weight of the selected metals suspended in wax. Normalized to 1 to compare the hardness of each spectrum.

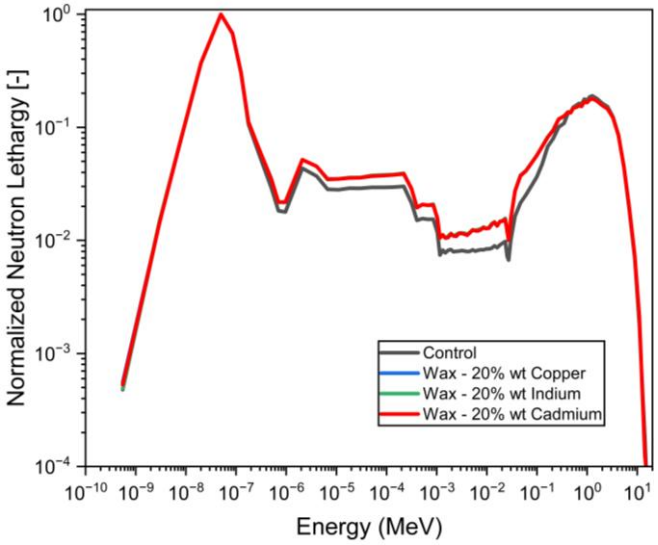

Fig. 11. Comparison of MCNP-generated neutron spectra in the drop tube location for 20% weight of the selected metals suspended in wax. Normalized to 1 to compare the hardness of each spectrum.

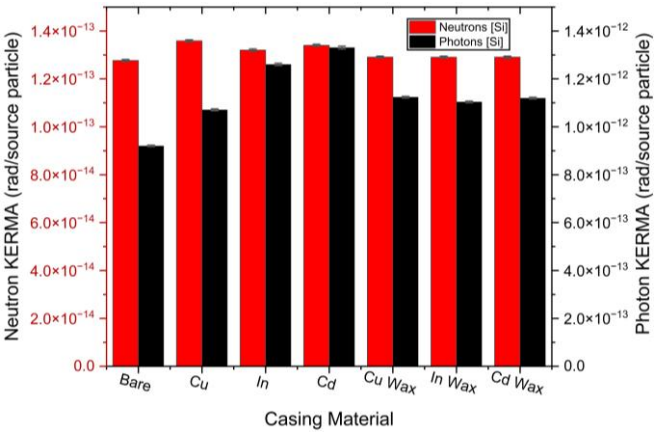

Fig. 12. MCNP-generated F6 energy deposition in silicon for the selected materials in the PUR-1 drop tube. Note the magnitude difference between the two axes of ordinates.

TABLE I
RELATIVE CHANGE IN ENERGY DEPOSITED INTO SILICON

Material	Relative Neutron Change (%)	Relative Photon Change (%)
Copper	6.43	16.40
Indium	3.40	36.97
Cadmium	4.96	44.62
Wax – Cu	1.11	22.14
Wax – In	1.08	19.97
Wax – Cd	1.10	21.70

The relative changes paired with the F6 tallies presented in Fig. 12 reveal that the MCNP model agrees with the first-principles model in that there is a preference for the metal sheets over the wax designs, excluding copper for both designs. The MCNP results show a full inversion in the order of the metals. This is most likely due to the inclusion of epithermal neutrons in the model. However, it is important to consider that the MCNP model does not include delayed gamma production, and the thermal scattering definition applied to the paraffin likely discounts the contribution of moderation from hydrogen. The first-principles model does not include full neutron energy information, scattering geometry, or gamma transport beyond the face of the casing. The MCNP model excludes delayed gammas and the paraffin thermal scattering. Together, this means that one model does not necessarily invalidate the other, but rather that the two models should be considered complementary. Specifically, they can be used as a starting place for determining the optimal geometry input and material selection for an experimental run.

V. ACTIVATION FOILS, DOSIMETRY, AND SAND-II

The thermoluminescent dosimeter is a standardized means of measuring the dose of a radiation environment. Lithium-fluoride (LiF) type TLDs are special in that the Li-6 isotope has an incredibly high affinity for neutrons *via* the (n,α) reaction relative to the Li-7 isotope. By manufacturing TLDs using different ratios of the isotopes, two types of dosimeters can be developed. Where a TLD-600 (Li-6 rich) is sensitive to neutrons and gammas, and a TLD-700 (Li-7 rich) is effectively sensitive to gammas [28, 29]. When used in tandem, these two TLDs can determine the dose contribution from gammas and neutrons separately. Thus, the TLD 600/700 pair is an ideal relative dosimeter for the fission environment, such that the LiF crystals are sized correctly so that the signal-to-noise ratio balances self-shielding and photon emission [27]. However, a neutron energy correction factor must be applied (K_n), which in itself is energy-dependent. Related to the energy correction is the self-shielding factor (f_{600}) that must be applied to the TLD-600 because the dose is overestimated from outer layers absorbing neutrons before interacting with the inner layers.

Similar to neutrons, photon corrections with LiF are a function of energy, but is dependent upon density as opposed to isotope. The NIST photon attenuation for LiF is used to determine the correction factors, where both the mass attenuation coefficient (μ/ρ) and mass-energy absorption coefficient (μ_{en}/ρ) are utilized for this work. The first value can be likened to the transparency of LiF to that photon energy, whereas the latter is the potential of a photon of a particular

energy to deposit energy in the form of secondary electrons into the medium [30].

The energy-dependent nature of both incident neutrons and photons in lithium fluoride requires a correction factor to be derived for the particles. Photons are straightforward since several isotopes or X-ray machines can be used to generate a monoenergetic photon source for calibration at various energies. An alternative is to calibrate the TLDs in a monoenergetic field with a known dose rate, such as Co-60, then use MCNP to create an energy relation curve for the deposited KERMA from various photon energies [31]. It should be noted that TLD dose is later reported as the "Co-60 reference," meaning that the energy correction for photons has not been applied. This was done because no mechanisms were used to experimentally collect energy information on the prompt gammas in the PUR-1 drop tube. However, future work using a high-purity germanium detector may be warranted. In that case, an energy-weighted correction factor will be applied.

Neutron correction factors, however, are difficult to establish due to the lack of a monoenergetic source. Consequently, there is significantly less experimental data, owing to the difficulty of producing well-characterized neutron fields and the energy-dependent nature of neutron moderation in any practical geometry. As a result, several experiments have been used to historically determine the differential KERMA for neutrons in various target materials. The most common, due to its prevalence, is neutron KERMA in human tissues, but due to the size, cost, and ease of use of the TLD, experimental data have been published for LiF. As stated previously, there are several orders of magnitude difference in thermal neutron interaction between Li-6 and Li-7, so the KERMA of each isotope must be handled separately. Fortunately, this is as simple as adding the differential KERMA of fluoride to the respective value of lithium-6 or lithium-7 [32].

However, the derivation of the neutron correction factors requires information related to the environmental neutron energy spectra in order to fold the neutron KERMA into a single value. To rectify the recursive nature of folding the KERMA, metal activation foils can be utilized and paired with neutron spectrum unfolding software. The iterative unfolding code SAND-II was used for this work. The methods outlined in ASTM E722-19 and ASTM E261-16 provide the technical details for selecting metal foils, individual foil corrections, and appendices for folding spectra into 1-MeV equivalent fluence in silicon. The key values that are extracted from the use of the ASTM manuals and SAND-II are the equivalent fluence in silicon, which can be used for comparing displacement damage potential in various facilities, and the differential neutron flux for correcting the TLD-reported dose. Iterative unfolding codes often require an *a priori* neutron spectrum as an initial estimate. MCNP is often used to generate this initial spectrum, but this further drives the recursive nature of correcting for neutron energy. The solution is to assume that one of the measurements is the ground truth. In this work, the bare PUR-1 spectrum is the *a priori*, and all further values are derivatives of this, corrected following their output from SAND-II. Beginning from a ground-truth a priori MCNP spectrum, the TLD-600 dose measured at the Co-60 reference is unfolded with SAND-II to obtain the neutron spectrum, which is written as an MCNP SDEF source to compute the TLD KERMA and, in turn, the 1 MeV equivalent fluence and TLD efficiency (η_{600}) that are compared back against the *a priori* spectrum.

The gamma and neutron doses in the mixed field can be determined under the following relationships,

$$D_\gamma = R_{700} K_\gamma \tag{27}$$

$$D_n = \frac{(R_{600} - R_{700}) K_\gamma}{K_n(E) \cdot \phi(E) \cdot f} \tag{28}$$

where D_n is the neutron KERMA, D_γ is the gamma dose at the Co-60 reference, R_{600} is the charge-correlated dose for the TLD-600, R_{700} is the charge-correlated dose for the TLD-700, and K_n and K_γ are the integrated neutron KERMA and gamma KERMA corrections, respectively. Finally, $\phi(E)$ is the differential neutron flux from SAND-II. Another useful metric for evaluating the performance of the TLD-600s in any neutron spectrum is the efficiency between the reported dose and the calculated KERMA. The efficiency,

$$\eta_{600} = \frac{(R_{600} - R_{700}) K_\gamma}{D_n} \tag{29}$$

is an indirect measurement of spectrum hardness, where values in the direction of unity are indicative of a more thermal spectrum.

Once the gamma dose is determined from the TLDs, the dose in the target material of interest can be related to the LiF dose using the Burlin cavity theory correction by means of the ratio between NIST tabulated photon stopping power (S) and mass-energy absorption coefficients for both materials

$$D_{target} = D_{LiF} \cdot \left[\left(\frac{\bar{S}}{\rho} \right)_{LiF}^{target} + (1 - d) \left(\frac{\overline{\mu_{en}}}{\rho} \right)_{LiF}^{target} \right] \tag{30}$$

where (d) is the cavity weighting parameter. Clinical studies have found that for the relevant energies, the value of the weight parameter ranges from 0.06 to 0.45 [33]. Table II provides the values for each casing design using the prompt gamma ray spectrum, including hydrogen for the wax designs. It should be noted that the stopping power ratio remains constant among the materials with a value of 0.995. Cavity theory is necessary to prevent under- or overestimating the dose in any particular test material. However, the true benefit is for a characterization of the environment relative to the TLD in which other non-silicon materials can be tested without the need for reestablishing the energy-dependent dose for any given test casing. This minimizes the risk of creating unnecessary activated material.

TABLE III
BURLIN CAVITY THEORY WEIGHTING FACTORS

Material	D (-)	μ_{en}/ρ (cm^2/g)	$E_{eff.}$ (MeV)
Bare	0.30	0.9288	1.76
Copper	0.45	0.9159	2.52
Indium	0.40	0.9219	2.21
Cadmium	0.06	0.9280	0.70
Wax – Cu	0.40	0.9219	2.21
Wax – In	0.37	0.9251	2.07
Wax – Cd	0.25	0.9309	1.55

VI. PUR-1 EXPERIMENT

The PUR-1 experiments consisted of seven trials. One was for characterizing the bare conditions, and the rest were the selected metal sheets and wax composites. Each material was placed in the drop tube for two separate runs at 20% reactor power for 20-minutes. The power and run time were selected to ensure that the indium exposure did not exceed 1 R/hr at 30 cm.

The first 20-minute run consisted of the metal activation foils (Au, In, Cu, Co, MnCu, NaCl, and Ni). The second run consisted of the non-shorted, unbiased BSS119N MOSFETS and 10 each of TLD-600 and TLD-700. This order was selected to maximize the delayed gamma ray production to the MOSFETs and dosimeters.

Two distinct challenges existed while constructing the test casings. For the metal sheets, it was difficult to find thicknesses that matched the simulated 0.6 cm. For the wax, it was difficult to create a homogeneous mixture due to differences in densities during the wax solidification process. The indium powder in particular would melt and coalesce at the bottom of the beaker during the mixing process despite the heating plate also having a stirrer. Despite the challenges, the metal sheets were selected to as closely match the simulated values, and all efforts were made to construct a homogeneous doped wax.

The activation foils were measured no more than 20 minutes after their removal from the neutron flux. The indium foil took precedence due to the limiting half-life. The MOSFETS were electrically characterized no more than 24 hours following their removal from the flux. While several tests were conducted on the FETs, for this work only the value of the threshold voltage (V_{TH}) was considered due to its highly cited correlation with TID. Finally, the TLDs were measured no more than 24 hours following removal. The resulting unfolded neutron spectrum for the metal sheets is shown in Fig. 13 and the wax composites in Fig. 14, where both instances are compared to the bare PUR-1 condition. It should be noted that these plots are neutron flux per unit lethargy, so they are plotted to show relative flux as opposed to relative hardness, as was the case in earlier sections.

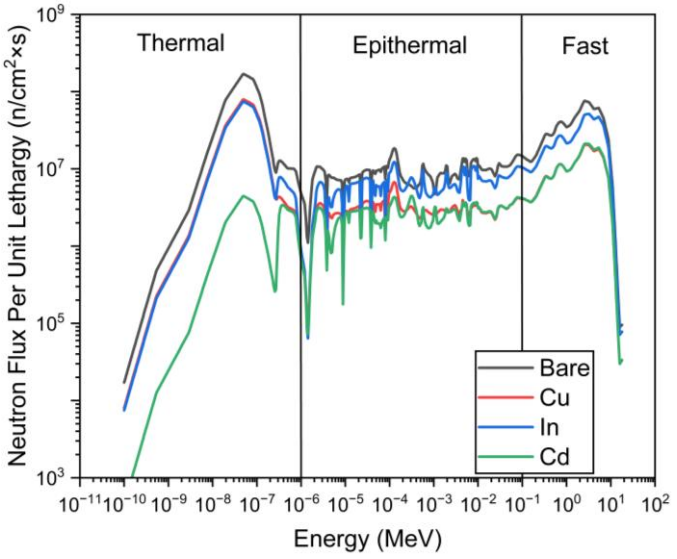

Fig. 13. SAND-II-derived neutron spectra for the selected metal sheets while in the PUR-1 drop tube corrected to 100% reactor power.

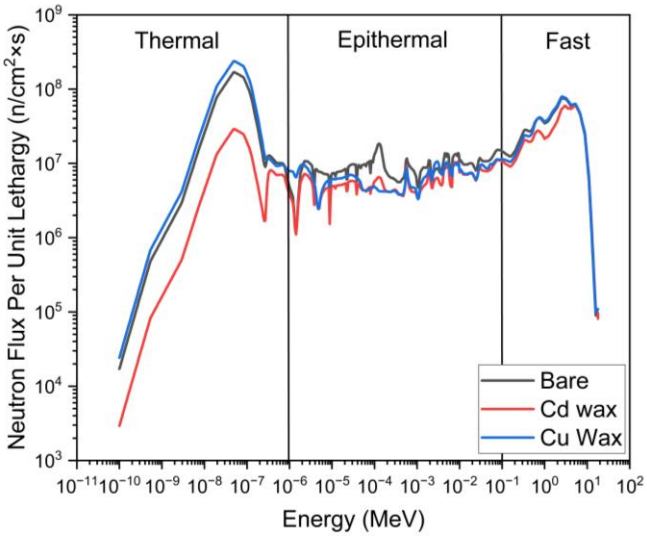

Fig. 14. SAND-II-derived neutron spectra for the selected wax composites while in the PUR-1 drop tube corrected to 100% reactor power.

The measured TLD dose for 20 minutes at 20% reactor power for each test casing material is shown in Table III. The TLD-reported photon dose at the Co-60 reference is a fair comparison among the test casing materials. Despite not being photon energy-corrected, at most this may add around 5% uncertainty to each reported value. However, the reported neutron values are not a fair comparison because they have not yet been spectrum-corrected, and the uncertainty may span several orders of magnitude. The spectrum- and self-shielding-corrected KERMA values are shown in Table IV along with the TLD-600 efficiency value, which can be used to compare the TLD response in each field. The measured photon dose and the calculated neutron KERMA in LiF are plotted in Fig. 15. These values can be directly compared to the MCNP F6 tallies plotted in Fig. 12. Similar characteristics can be derived for the 1-MeV equivalent fluence in silicon as well as the photon dose. These values are displayed in Table V.

TABLE III
THERMOLUMINESCENT DOSIMETER MEASURED DOSES IN COBALT-60

Material	Photon Dose (krads [LiF])	Neutron Dose (krads [LiF])
Bare	$4.95\times10^{0} \pm 8.60\times10^{-2}$	$3.29\times10^{0} \pm 1.44\times10^{-1}$
Copper	$6.59\times10^{0} \pm 7.71\times10^{-1}$	$2.49\times10^{0} \pm 1.14\times10^{-1}$
Indium	$5.98\times10^{0} \pm 9.35\times10^{-1}$	$1.52\times10^{0} \pm 1.57\times10^{-1}$
Cadmium	$2.41\times10^{0} \pm 6.11\times10^{-1}$	$4.84\times10^{-1} \pm 9.19\times10^{-2}$
Wax – Cu	$7.19\times10^{0} \pm 1.01\times10^{-1}$	$1.22\times10^{0} \pm 1.36\times10^{-1}$
Wax – In	TBD	TBD
Wax – Cd	$3.64\times10^{0} \pm 5.53\times10^{-2}$	$1.49\times10^{0} \pm 7.95\times10^{-2}$

TABLE IV
CALCULATED NEUTRON KERMA AND EFFICIENCY IN TLD-600

Material	Neutron KERMA (krads [LiF])	η_{600} (-)
Bare	$7.79\times10^{1} \pm 2.80\times10^{0}$	$4.22\times10^{-2} \pm 2.41\times10^{-3}$
Copper	$1.97\times10^{1} \pm 8.75\times10^{-1}$	$1.26\times10^{-1} \pm 8.06\times10^{-3}$
Indium	$3.55\times10^{1} \pm 1.76\times10^{0}$	$4.28\times10^{-2} \pm 4.91\times10^{-3}$
Cadmium	$3.58\times10^{0} \pm 1.42\times10^{-1}$	$1.35\times10^{-1} \pm 2.62\times10^{-2}$
Wax – Cu	$1.15\times10^{2} \pm 5.77\times10^{0}$	$1.06\times10^{-2} \pm 1.18\times10^{-3}$
Wax – In	TBD	TBD
Wax – Cd	$1.73\times10^{1} \pm 8.28\times10^{-1}$	$8.61\times10^{-2} \pm 6.17\times10^{-3}$

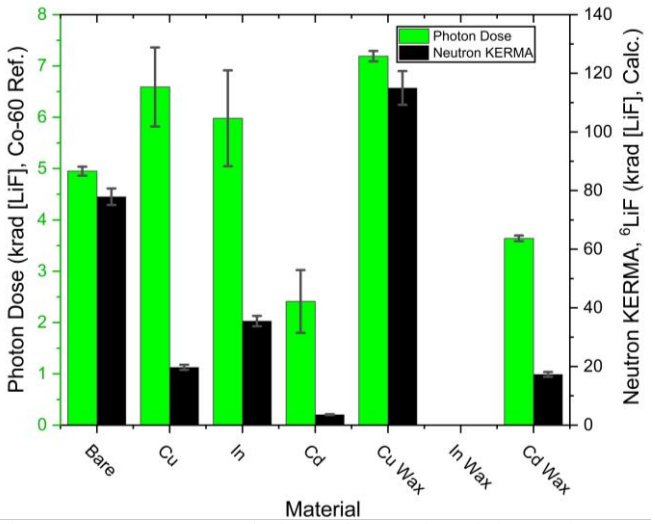

Fig. 15. TLD-700 measured photon dose at the cobalt-60 reference and corrected neutron KERMA derived from TLD-600/700 pair for each casing material in PUR-1.

TABLE V
RADIATION ENVIRONMENTS IN SILICON

Material	1-MeV Equivalent Fluence (n/cm^2)	Photon Dose (krads [Si])
Bare	$2.27\times10^{11}\pm6.71\times10^{9}$	$5.22\times10^{0}\pm1.81\times10^{-1}$
Copper	$1.63\times10^{11}\pm8.11\times10^{9}$	$6.93\times10^{0}\pm8.37\times10^{-1}$
Indium	$1.25\times10^{11}\pm6.23\times10^{9}$	$6.23\times10^{0}\pm1.00\times10^{0}$
Cadmium	$1.86\times10^{10}\pm9.16\times10^{8}$	$2.59\times10^{0}\pm6.60\times10^{-1}$
Wax – Cu	$2.47\times10^{11}\pm1.21\times10^{10}$	$7.56\times10^{0}\pm2.50\times10^{-1}$
Wax – In	TBD	TBD
Wax – Cd	$1.95\times10^{11}\pm9.59\times10^{9}$	$3.84\times10^{0}\pm1.29\times10^{-1}$

The MOSFET threshold voltage characteristics are compared to the unirradiated control for each of the environments in Table VI. Although each run consisted of 10 irradiated devices, 4 were withheld from the measurement to study time-dependent effects, and the remainder were used to generate data. The most interesting aspect of the MOSFET threshold voltage shift occurs when comparing the correlation between the reported photon dose in silicon and the calculated thermal neutron fluence. Where the thermal fluence is found by integrating the differential neutron fluence for neutron energies below 0.5 eV. While both the photon dose and thermal fluence have a collinear effect on V_{TH}, the linear regression provides evidence that the shift in V_{TH} correlates more strongly with thermal neutron fluence than with measured photon dose. This comparison is conducted by normalizing each environment to the respective bare condition of either thermal fluence or photon dose, then plotted against ΔV_{TH}. The correlation is plotted in Fig. 16.

TABLE VI
MOSFET THRESHOLD VOLTAGE IN VARIOUS CASINGS

Material	V_{TH} (V)	ΔV_{TH} from Control (mV)
Control	$2.16\times10^{0}\pm1.39\times10^{-2}$	N/A
Bare	$2.01\times10^{0}\pm1.11\times10^{-2}$	$-1.49\times10^{3}\pm1.78\times10^{1}$
Copper	$2.05\times10^{0}\pm2.33\times10^{-2}$	$-1.13\times10^{3}\pm2.71\times10^{1}$
Indium	$2.04\times10^{0}\pm2.44\times10^{-2}$	$-1.23\times10^{3}\pm2.81\times10^{1}$
Cadmium	$2.07\times10^{0}\pm4.02\times10^{-3}$	$-8.60\times10^{2}\pm1.45\times10^{1}$
Wax – Cu	$1.97\times10^{0}\pm1.39\times10^{-2}$	$-1.86\times10^{3}\pm1.97\times10^{1}$
Wax – In	TBD	TBD
Wax – Cd	$2.07\times10^{0}\pm4.64\times10^{-2}$	$-8.53\times10^{2}\pm4.84\times10^{1}$

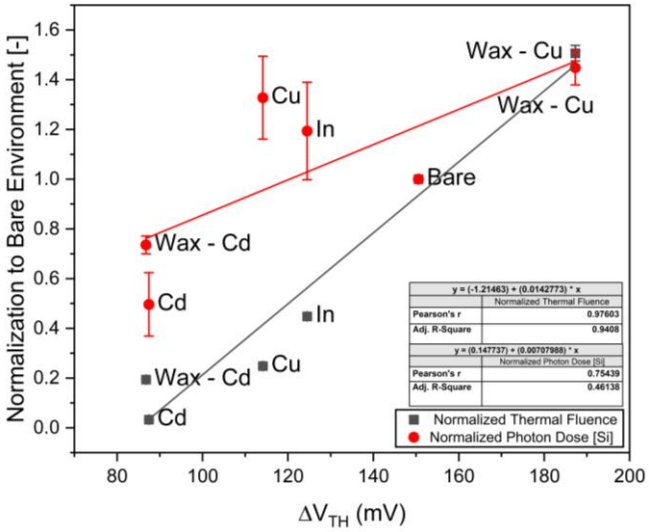

Fig. 16. Comparison of V_{TH} to thermal neutron fluence and photon dose in silicon normalized to bar condition. Note the larger correlation to thermal neutron flux over photon dose.

VII. DISCUSSION

The motivation for this work was the shortfall in availability in MIL-STD-883 compliant facilities for conducting radiation tests. The addition of cadmium sheets over the DUT in an attempt to harden the neutron spectrum for displacement damage evaluation provided evidence that the thermal neutron fluence had a non-negligible effect on the performance of the MOSFET used in the test. It was then of interest to see if different metals could tailor the fission spectrum for either displacement damage testing or TID testing. While TRIGA reactors are the only thermal reactors approved for MIL-STD qualification, PUR-1 offered an opportunity to determine if the experimenter had to accept the neutron energy distribution and the photon dose as is, or if they could be tailored to the needs of the project. The results in this work show strong evidence for the latter.

The methods presented here provide a first-order, figure-of-merit approach to selecting conversion materials and optimal thickness based on limited knowledge of the incident neutron spectrum. The rough approximation of the fast-to-thermal neutron ratio is required, which can be collected with a gold foil experiment in under 1-hour. Unfortunately, the highly thermalized neutron spectrum and limited volume in the PUR-1 drop tube reduced the wax in the layered design to zero thickness, resulting in a pure metal sheet. This means that the full utility of the algorithm has yet to be explored and warrants a fast source and an unrestricted space for testing.

There was severe disagreement between the first-principles-derived algorithm and the same geometry modeled in MCNP. As described briefly above, both models omit physical phenomena that were observed experimentally. Considering only the photon dose, the first-principles model better aligned with the experimental data than MCNP, reproducing the measured ordering of Cu > In > Cd, whereas the Monte Carlo results inverted it. The most likely reason is that the figure of merit for converter B carries the escape probability explicitly, integrating the local capture rate against $e^{(-\mu(E)(L-x))}$ over the casing thickness, so a cascade concentrated at low energy is

penalized for failing to reach the target. Cadmium is the extreme case: its capture cross section is large enough that the reaction rate is confined to the first fraction of a millimeter, and the dominant 558.6 keV line must then traverse the full remaining thickness. Copper, with a macroscopic absorption cross section more than two orders of magnitude smaller, distributes capture throughout the sheet and emits a harder cascade that escapes more readily. However, this does not invalidate the MCNP model. The two treatments fail in different directions and are best regarded as bounding cases: the analytic model neglects scattering geometry and gamma transport beyond the casing face, while the Monte Carlo model transports photons rigorously but includes only prompt emission, omitting the delayed contribution from Cu-64 and In-116m that accrues over a twenty-minute irradiation and persists into the subsequent dosimetry run. For casing selection, the analytic figure of merit is the more useful screening tool because it is inexpensive to evaluate across thickness and correctly captures self-attenuation; MCNP remains necessary for absolute dose prediction and for any geometry where scattering from surrounding structures is significant.

Measured experimental results identified copper-doped paraffin wax as the best conversion material, providing an approximate dose in silicon of 32 rad(Si)/s at 100% reactor power compared to the MIL-STD's 50 rad(Si)/s floor. This dose rate represents a 44.8% increase from the bare condition. Providing evidence that the PUR-1 reactor can be used to modify the photon dose rate in a way that does not replace, but approaches, the Co-60 standard. However, the 1-MeV equivalent neutron fluence requires that the TID be less than 500 rad(Si) per 1×10^{12} n/cm^2 fluence. While each casing environment could provide this fluence given enough time, the most conservative condition (Cd-wax) exceeds this TID limit by a factor of 39.4, and the worst case (pure Cd) by a factor of 278.5. This means that at its current position in the reactor pool, the drop tube could only ever act as a TID test, but would not come close to replacing the displacement damage standard. One note worth mentioning is related to the activation foils for the threshold reactions Ni-58(n,p)Co-58 and In-115(n,n')In-115m, which is that their counting statistics were poor. These reactions specifically tie the fast region in the SAND-II unfolding code. Longer irradiation time would fix this problem, but the activation of the test casings is limited by both reactor power and irradiation time set internally by Purdue regulations. The poor counting statistics for these foils most likely affected the cadmium sheet environment the most, given that a large portion of the thermal signal was removed. This results in the epithermal neutrons providing the majority of the input into SAND-II, and this is apparent in the unfolded spectrum given the large variances in the epithermal region correlated to resonances in the activation foils. The consequence is most evident in the cadmium 1-MeV equivalent fluence of 1.86×10^{10} n/cm², a 92% reduction from bare, which is difficult to attribute to a material nearly transparent to fast neutrons and therefore likely an unfolding artifact. The 278.5× ratio should be treated as provisional.

Although PUR-1 cannot substitute for the MIL-STD neutron displacement test, this reactor does provide a unique environment for testing thermal neutron fluence, which has historically and intentionally been removed from rad-hard experiments by using a fast source or cadmium shielding. However, as the demand for digital sensors integrated into reactor instrumentation and control increases, so does the demand for testing thermal neutron effects on microelectronics. This demand may be driven by in-core sensors for small modular reactors and spent-fuel monitoring, where MIL-STD-750/883 have historically focused on weapons and space environmental effects, both fast-dominated fields. This makes a reactor like PUR-1 the ideal testing environment for up-and-coming sensors. The BSS119N MOSFETs' threshold voltage correlated more strongly with thermal fluence (R^2=0.94) than with photon dose in silicon (R^2=0.46), though the two covary, and this data cannot isolate the responsible mechanism. However, it raises the question if the MIL-STD-883 testing requirements are relevant for systems intended to be in proximity to thermal sources.

It is unknown at this time if the BSS119N contains a significant enough amount of boron-10 to have relevant thermal damage effects from the thermal fluence. Therefore, future work is required to classify the boron content in the p-type regions through methods like the Mott-Schottky analysis. If confirmed, this would identify the mechanism behind the discrepancy between externally measured dose and dose generated internally to the DUT. As digital nuclear sensors composed of commercial parts proliferate the market, they should be considered for testing in thermal fluence, or at the very least, have their boron content disclosed before being placed in a system that may be subjected to neutrons of relevant energies.

VIII. Conclusion

This work demonstrates that thermal reactor facilities can help alleviate the limited availability of large-scale radiation testing facilities such as the National Ignition Facility or the White Sands Missile Range Fast Burst Reactor. While a radiation test within a thermal reactor cannot replace the qualification standards outlined in MIL-STD-883, it may offer a supplemental method conducted more frequently and earlier in the design process for systems requiring a radiation-hardened designation.

A first-principles figure of merit was developed to select conversion materials and thicknesses from limited knowledge of the incident spectrum, and was compared against MCNP6.3 and against measurements in PUR-1. Copper-doped paraffin produced the highest measured photon dose in silicon, 32 rad(Si)/s at full reactor power and 44.8% above the bare drop tube. The measured material ordering matched the analytic model rather than the Monte Carlo result, indicating that self-attenuation of the capture cascade governs which materials perform well in a highly thermalized field.

The threshold voltage shift of the BSS119N MOSFETs correlated more strongly with thermal neutron fluence than with the externally measured photon dose, and cadmium shielding that removed 97% of the thermal fluence also removed 42% of the shift. Because the two quantities covary, this data cannot isolate the responsible mechanism, but the result indicates that dose generated internal to a device may go unrecorded by dosimetry placed alongside it. This is directly relevant to commercial parts intended for reactor instrumentation, where

thermal neutrons are present and where existing hardness assurance practice deliberately excludes them.

Future work will determine the boron content of the device through depth-resolved elemental analysis, improve fast-group counting statistics to constrain the unfolded spectra, and separate the thermal and photon contributions through exposures in which the two are varied independently. Additional work will address material homogeneity within wax composites and time-dependent activation effects.

DISCLAIMER

The views expressed are those of the authors and do not reflect the official guidance or position of the United States Government, the Department of War, the United States Air Force, or the United States Space Force.

ACKNOWLEDGMENT

This work heavily relies on the efforts of Major David Fobar, Major Adam Card, and LTC Andrew Decker of the Nuclear Science & Engineering Research Center at West Point, New York. True Miller and Brian Jowers III of the PUR-1 Research facility have been instrumental in gathering data. Also of Note, Dr. Linda Nie, Nathan Claus and Purdue's Environmental Health and Safety team for dosimetry preparation.

REFERENCES

[1] National Academies of Sciences, Engineering, and Medicine, *Testing at the Speed of Light: The State of U.S. Electronic Parts Space Radiation Testing Infrastructure*. Washington, DC, USA: National Academies Press, 2018.

[2] *Test Method Standard: Microcircuits*, MIL-STD-883H, Dept. of Defense, Washington, DC, USA, 2010.

[3] M. Niichel *et al.*, "Design and characterization of the modified Purdue subcritical pile for nuclear research applications," *Instruments*, vol. 9, no. 2, 2025, Art. no. 13, doi: 10.3390/instruments9020013.

[4] M. Niichel, T. Miller, B. Jowers, R. Cooper, and S. Chatzidakis, "Response of boost converters under fission-spectrum neutron and gamma radiation," *IEEE Trans. Nucl. Sci.*, vol. 73, no. 1, pp. 110–119, Jan. 2026, doi: 10.1109/TNS.2025.3646921.

[5] M. Niichel and S. Chatzidakis, "Methodology for the evaluation of critical components of the SCatterable radiation monitor under radiation fields," 2025, *arXiv:2503.08754*.

[6] *Standard Guide for Selection and Use of Neutron-Activation Foils for Determining Neutron Spectra Employed in Radiation-Hardness Testing of Electronics*, ASTM E720-23, ASTM International, West Conshohocken, PA, USA, 2023, doi: 10.1520/E0720-23.

[7] *Standard Practice for Application of Thermoluminescence-Dosimetry (TLD) Systems for Determining Absorbed Dose in Radiation-Hardness Testing of Electronic Devices*, ASTM E668-20, ASTM International, West Conshohocken, PA, USA, 2020.

[8] J. E. Bevins *et al.*, "Performance evaluation of an energy tuning assembly for neutron spectral shaping," *Nucl. Instrum. Methods Phys. Res. A, Accel. Spectrom. Detect. Assoc. Equip.*, vol. 923, pp. 79–87, Apr. 2019, doi: 10.1016/j.nima.2019.01.049.

[9] *Standard Practice for Characterizing Neutron Fluence Spectra in Terms of an Equivalent Monoenergetic Neutron Fluence for Radiation-Hardness Testing of Electronics*, ASTM E722-19, ASTM International, West Conshohocken, PA, USA, 2019.

[10] K. R. DePriest, "Historical examination of the ASTM standard E722 1-MeV silicon equivalent fluence metric," Sandia Nat. Lab., Albuquerque, NM, USA, Rep. SAND2019-15194, 2019.

[11] J. E. Bevins, "Targeted modification of neutron energy spectra for national security applications," Ph.D. dissertation, Dept. Nucl. Eng., Univ. California, Berkeley, CA, USA, 2017.

[12] W. Kloppenburg, "Neutron spectral effect on microelectronic device performance," M.S. thesis, Dept. Eng. Phys., Air Force Inst. Technol., Wright-Patterson AFB, OH, USA, Rep. AFIT-ENG-MS-20-90210, 2022.

[13] D. Lv, Y. Gao, and S. Zhou, "Study on irradiation effects and degradation model of bipolar junction transistor under severe-accident conditions in nuclear power plants," *Prog. Nucl. Energy*, vol. 199, Sep. 2026, Art. no. 106489, doi: 10.1016/j.pnucene.2026.106489.

[14] C. Townsend, "Technical specifications for the Purdue University reactor PUR-1," Purdue Univ., West Lafayette, IN, USA, Rep. 50-182, 2018.

[15] A. F. Henry, *Nuclear Reactor Analysis*. Cambridge, MA, USA: MIT Press, 1975.

[16] A. Koning, M. Chadwick, and Hetrick, "Copper-65 neutron total cross section," ENDF/B-VIII.0, 2016.

[17] A. Koning, M. Chadwick, and Hetrick, "Copper-63 neutron total cross section," ENDF/B-VIII.0, 2016.

[18] W. G. Mughabghab, "Cadmium-113 neutron total cross section," ENDF/B-VIII.0, 2010.

[19] W. G. Mughabghab, "Indium-115 neutron total cross section data," Mar. 8, 2024. [Online]. Available: https://www-nds.iaea.org/exfor/servlet/X4sShowData?db=x4&op=get_plotdata&req=-1&ii=42&File=E4R10339_e4.zvd.dat.txt

[20] S. Seltzer, "Tables of X-ray mass attenuation coefficients and mass energy-absorption coefficients," Nat. Inst. Standards Technol., Gaithersburg, MD, USA, NIST Standard Reference Database 126, 1995, doi: 10.18434/T4D01F.

[21] R. C. Reedy and S. C. Frankle, "Prompt gamma rays from radiative capture of thermal neutrons by elements from hydrogen through zinc," *At. Data Nucl. Data Tables*, vol. 80, no. 1, pp. 1–34, Jan. 2002, doi: 10.1006/adnd.2001.0870.

[22] T. Miller, "Production of lutetium-177 via the indirect route using PUR-1," M.S. thesis, Purdue Univ., West Lafayette, IN, USA, 2021.

[23] J. Verbeke, C. Hagmann, and D. Wright, "Simulation of neutron and gamma ray emission from fission," Lawrence Livermore Nat. Lab., Livermore, CA, USA, Rep. UCRL-AR-228518, 2010.

[24] M. Hricova, M. Petkova, Z. Tomcikova, and A. Ujhelyiova, "The effect of inorganic pigments on the rheological properties of the color masterbatches from polylactic acid," *Fibers*, vol. 13, no. 9, Sep. 2025, Art. no. 122, doi: 10.3390/fib13090122.

[25] S. Murray, E. Jones, C. Winters, A. Ramirez, and S. Davis, "Exploring the process-structure-property relationship of aerosol deposition to phosphor coatings for non-contact thermometry," Sandia Nat. Lab., Albuquerque, NM, USA, Rep. SAND2023-13163, 2023.

[26] T. Ahmed, B. K. Laramee, and A. I. Hawari, "Thermal scattering law data development for paraffin wax," *Trans. Amer. Nucl. Soc.*, vol. 129, no. 1, pp. 693–696, Nov. 2023.

[27] G. F. Knoll, *Radiation Detection and Measurement*, 4th ed. Hoboken, NJ, USA: Wiley, 2010.

[28] G. M. Hale, "Neutron total cross section, Li-6(n,tot)," ENDF/B-VIII.0.

[29] P. G. Young, "Neutron total cross section, Li-7(n,tot)," ENDF/B-VIII.0, Aug. 1988.

[30] "Lithium fluoride X-ray mass coefficient," Nat. Inst. Standards Technol., Gaithersburg, MD, USA. [Online]. Available: https://physics.nist.gov/PhysRefData/XrayMassCoef/ComTab/lithiumflu.html

[31] A. A. Nunn, S. D. Davis, J. A. Micka, and L. A. DeWerd, "LiF:Mg,Ti TLD response as a function of photon energy for moderately filtered x-ray spectra in the range of 20–250 kVp relative to ^{60}Co," *Med. Phys.*, vol. 35, no. 5, pp. 1859–1869, May 2008, doi: 10.1118/1.2898137

[32] R. S. Caswell, J. J. Coyne, and M. L. Randolph, "Kerma factors for neutron energies below 30 MeV," *Radiat. Res.*, vol. 83, no. 2, pp. 223–234, Aug. 1980, doi: 10.2307/3575276.

[33] E. Kearsley, “A new general cavity theory,” *Phys. Med. Biol.*, vol. 29, no. 10, pp. 1179–1187, Oct. 1984, doi: 10.1088/0031-9155/29/10/001.